

## SUPPORTING INFORMATION

---

### Supporting Information

#### **A Sterically Hindered D-A-D' Thermally Activated Delayed Fluorescence Emitter for Highly-Efficient Non-doped Organic Light-Emitting Diodes**

Zhan Yang,<sup>†</sup> Zhu Mao,<sup>†</sup> Chao Xu, Xiaojie Chen, Juan Zhao,<sup>\*</sup> Zhiyong Yang, Yi Zhang,<sup>\*</sup> William Wu, Shibo Jiao, Yang Liu, Matthew. P. Aldred, and Zhenguo Chi<sup>\*</sup>

**Abstract:** Thermally activated delayed fluorescence (TADF) materials have opened up a new chapter for high-efficiency and low-cost organic light-emitting diodes (OLEDs). Herein, we describe a novel and effective design strategy for TADF emitters by introducing a carbazole donor unit at the *ortho*-position, in which the donor and acceptor groups are in spatially-close proximity to guarantee the existence of intramolecular electrostatic attractions and space charge transfer, leading to reduced structural vibrations, suppressed non-radiative decay and rapid radiative decay to avoid excited state energy loss. As a result, a green TADF emitter (**2Cz-DPS**) showing high solid-state photoluminescence quantum efficiency (91.9%), and excellent OLED performance. Theoretical simulations reveal that the non-adiabatic coupling accelerates the reverse intersystem crossing of **2Cz-DPS**, resulting in the fabrication of a state-of-the-art non-doped OLED with extremely high external quantum efficiency of 28.7%.

## SUPPORTING INFORMATION

### Table of Contents

<b>I. Experimental Section</b> .....	3
<b>II. Synthesis and characterization</b> .....	4
<b>III. Supplementary Figures</b> .....	6
<b>Figure S1.</b> <sup>1</sup> H NMR spectra of <b>2-FSBr</b> . .....	6
<b>Figure S2.</b> <sup>1</sup> H NMR spectra of <b>2-CzSBr</b> . .....	7
<b>Figure S3.</b> EI-mass spectrum of <b>2-CzSBr</b> . .....	7
<b>Figure S4.</b> <sup>1</sup> H NMR spectra of <b>2Cz-DPS</b> . .....	8
<b>Figure S5.</b> <sup>13</sup> C NMR spectra of <b>2Cz-DPS</b> . .....	9
<b>Figure S6.</b> EI-mass spectrum of <b>2Cz-DPS</b> . .....	10
<b>Figure S7.</b> High resolution mass spectrum of <b>2Cz-DPS</b> . .....	10
<b>Figure S8.</b> CHN analytical of <b>2Cz-DPS</b> . .....	11
<b>Figure S9.</b> <sup>1</sup> H NMR spectra of <b>4Cz-DPS</b> . .....	12
<b>Figure S10.</b> (a) PL intensity of <b>2Cz-DPS</b> as a function of water ratio. (b) Effective diameters of <b>2Cz-DPS</b> nanoaggregates in H <sub>2</sub> O/THF mixtures with 90% water ratio. ....	13
<b>Figure S11.</b> (a) Reduced density gradient (RDG) isosurface map with isovalue of 0.5, and (b) HOMO and LUMO distribution of <b>4Cz-DPS</b> , showing the overlap integral extents $I_{H/L}$ . .....	14
<b>Figure S12.</b> (a) Transient and (b) delayed curves of <b>4Cz-DPS</b> and <b>2Cz-DPS</b> films. ....	14
<b>Figure S13.</b> PL spectra of (a) <b>4Cz-DPS</b> and (c) <b>2Cz-DPS</b> in different solvents. Linear correlation of orientation polarization ( $f$ ) of solvent media with the Stokes shift ( $\nu_a - \nu_f$ ) for (b) <b>4Cz-DPS</b> and (d) <b>2Cz-DPS</b> . ....	15
<b>Figure S14.</b> UV-vis absorption spectra of (a) <b>4Cz-DPS</b> and (b) <b>2Cz-DPS</b> in different solvents. ....	15
<b>Figure S15.</b> UV-vis absorption and PL spectra of <b>4Cz-DPS</b> and <b>2Cz-DPS</b> in (a) neat films and (b) THF solutions. ....	16
<b>Figure S16.</b> (a) Variable-temperature steady-state spectra and (b) transient PL decay curves of <b>2Cz-DPS</b> films carried out at different temperatures. ....	17
<b>Figure S17.</b> (a) Variable-temperature steady-state spectra and (b) transient PL decay curves of <b>4Cz-DPS</b> films carried out at different temperatures. ....	17
<b>Figure S18.</b> PL spectra of (a) <b>4Cz-DPS</b> and (b) <b>2Cz-DPS</b> films in air and vacuum. ....	18
<b>Figure S19.</b> Fluorescence spectra at room temperature and phosphorescence spectra at 77 K for <b>4Cz-DPS</b> and <b>2Cz-DPS</b> films. ....	18
<b>Figure S20.</b> Natural transition orbitals of <b>4Cz-DPS</b> for the $S_0$ , $S_1$ , $T_1$ , $T_2$ , $T_3$ and $T_4$ states. ....	19
<b>Figure S21.</b> Natural transition orbitals of <b>2Cz-DPS</b> for the $S_0$ , $S_1$ , $T_1$ , $T_2$ , $T_3$ , $T_4$ and $T_5$ states. ....	20
<b>Figure S22.</b> (a) Cyclic voltammetry measurements of <b>4Cz-DPS</b> and <b>2Cz-DPS</b> . (b) UV-absorption spectra in DCM solutions ( $5 \times 10^{-4}$ mol/L) of <b>4Cz-DPS</b> and <b>2Cz-DPS</b> . ....	21
<b>Figure S23.</b> (a) Thermogravimetric analysis curves and (b) differential scanning calorimetry curve of <b>4Cz-DPS</b> and <b>2Cz-DPS</b> measured under N <sub>2</sub> , showing the glass transition temperature ( $T_g$ ). ....	21
<b>Figure S24.</b> EQE–luminance curves of other five <b>2Cz-DPS</b> devices. ....	22
<b>Figure S25.</b> Current density–voltage curves of (a) <b>4Cz-DPS</b> and (b) <b>2Cz-DPS</b> based single carrier devices. ....	23
<b>Figure S26.</b> EQE–current density curve simulation for (a) <b>2Cz-DPS</b> device and (b) <b>4Cz-DPS</b> device. ....	24
<b>IV. References</b> .....	24
<b>Author Contributions</b> .....	25

# SUPPORTING INFORMATION

## I. Experimental Section

**General Methods.** Hydrogen ( $^1\text{H}$ ) and carbon ( $^{13}\text{C}$ ) nuclear magnetic resonance (NMR) spectra were measured using a Bruker AvanceIII spectrometer, with deuterated dimethylsulfoxide ( $\text{DMSO-}d_6$ ) and chloroform ( $\text{CDCl}_3$ ) as solvents and tetramethylsilane (TMS) as an internal reference. Electron impact-mass spectra (EI-MS) and high resolution mass spectra (HRMS) were collected from Thermo DSQ spectrometer and Thermo MAT95XP spectrometer, respectively. Elemental analysis was conducted using an Elementar Vario EL analyzer. Transient photoluminescence (PL) decay characteristics, time-resolved phosphorescence spectra and PL quantum yields were recorded on a Horiba JY FL-3 spectrometer equipped with a calibrated integrating sphere. PL spectra and UV-vis absorption spectra were measured using a Shimadzu RF-5301PC spectrometer and a Hitachi U-3900 spectrophotometer, respectively. Differential scanning calorimetry (DSC) was performed using a NETZSCH DSC 204 F1 thermal analyzer at a heating rate of  $10\text{ }^\circ\text{C min}^{-1}$  under a  $\text{N}_2$  atmosphere. Thermogravimetric analyses (TGA) were performed with a TA thermal analyzer (A50) under a  $\text{N}_2$  atmosphere with a heating rate of  $20\text{ }^\circ\text{C min}^{-1}$ . Cyclic voltammetry measurements were carried out on an electrochemical workstation VMP300 (Bio-Logic), by using tetrabutylammoniumhexafluorophosphate ( $\text{TBAPF}_6$ , 0.1 M) in dichloromethane as electrolyte, a platinum as counter electrode, and a  $\text{Ag}/\text{AgCl}$  as reference electrode (versus ferrocene  $\text{F}_c/\text{F}_c^+$ ). All of the simulation calculations were carried out based on single crystal conformation with Gaussian 09W program package and produced by B3LYP/6-31G(\*). RDG analysis was obtained by Multiwfn (version 3.5) and plotted by VMD (version 1.9.3). Single-crystal X-ray data were determined using an Oxford Diffraction Gemini S Ultra X-ray Single Crystal Diffractometer with a (Cu) X-ray source. Single crystals were obtained through slow evaporation of saturated solution consisting of ethanol and dichloromethane mixed solvents (CCDC number of **2Cz-DPS** and **4Cz-DPS** is 1891672 and 981368 respectively).

**Materials.** Poly(3,4-ethylenedioxythiophene):poly(styrenesulfonate) (PEDOT:PSS), m-bis(N-carbazolyl)benzene (MCP) and 1,3,5-tris(N-phenylbenzimidazol-2-yl)benzene (TPBI) were used as purchased from Xi'an Polymer Light Technology Co. Ltd. All the chemicals were used as received without any purification. The TADF material **4Cz-DPS** was reported in our previous work.<sup>[1,2]</sup>

**Devices Fabrication and Characterization.** Indium tin oxide (ITO) coated glass substrates with a sheet resistance of  $8\ \Omega\ \text{sq}^{-1}$  were ultrasonically cleaned to use as the anode. Subsequently, PEDOT:PSS was spin-coated on the cleaned ITO at a speed of 2000 rpm for 60 seconds, following by thermal annealing for 15 minutes at  $200\text{ }^\circ\text{C}$  under atmospheric environment to afford 30 nm thickness. Then, the PEDOT:PSS coated ITO substrates were transferred to a thermal evaporation chamber, wherein the organic layers and metal cathode were sequentially deposited under vacuum pressure of  $4 \times 10^{-4}\ \text{Pa}$ , leading to an active area of  $20\ \text{mm}^2$  ( $2\ \text{mm} \times 10\ \text{mm}$ ). The current density–voltage–luminance characteristics and electroluminescence (EL) spectra of the OLEDs were measured using a Keithley 2400 source combined with a Photo Research PR735 spectrometer under room temperature, while the external quantum efficiencies (EQEs) were calculated using a computer program based on previously reported theory.<sup>[3]</sup>

**TADF Parameters Estimation.** The key rate constants and efficiencies of TADF process were calculated based on the following equations (1) – (4):<sup>[4]</sup>

$$k_{PF} = \frac{\phi_{PF}}{\tau_{PF}} \quad (1)$$

## SUPPORTING INFORMATION

$$k_{DF} = \frac{\phi_{DF}}{\tau_{DF}} \quad (2)$$

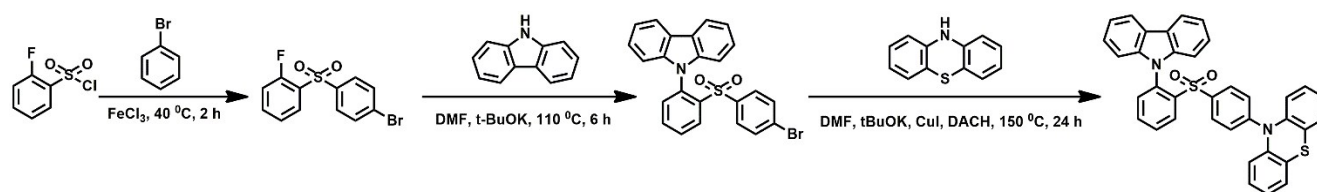
$$k_{ISC} = \frac{\phi_{DF}}{\phi_{PF} + \phi_{DF}} \cdot k_{PF} \quad (3)$$

$$k_{RISC} = \frac{k_{DF}k_{PF}}{k_{ISC}} \cdot \frac{\phi_{DF}}{\phi_{PF}} \quad (4)$$

where  $\phi_{PF}$  and  $\phi_{DF}$  are the quantum efficiency of prompted and delayed emissions respectively,  $\tau_{PF}$  and  $\tau_{DF}$  are the prompted and delayed emission lifetimes respectively,  $k_{PF}$  and  $k_{DF}$  are rate constant of prompted and delayed emissions respectively,  $k_{ISC}$  and  $k_{RISC}$  are the rate constant of intersystem crossing and reverse intersystem crossing respectively for the triplet excited states.

## II. Synthesis and characterization

2Cz-DPS was synthesized as below.



Scheme S1. Synthetic route of 2Cz-DPS.

### *Synthesis of 1-fluoro-2-((4-bromophenyl)sulfonyl)benzene (2-FSBr)*

2-fluorobenzenesulfonyl chloride (2.0 g, 10.28 mmol) and bromobenzene (3.2 g, 20.55 mmol) were dissolved in dichloromethane (10 ml), then Ferric chloride (2.2 g, 13.56 mmol) was added. The reaction mixture was stirred at 40 °C for 2 h. The reaction mixture was cooled to room temperature and quenched with 30 ml of 1 M HCl. The mixture was extracted with dichloromethane (20 ml  $\times$  3), washed with water and dried with anhydrous sodium sulfate. The product was obtained through filtration and solvent evaporation under reduced pressure. Compound 2-FSBr was obtained as a white powder in 83% yield (2.68 g).  $^1\text{H}$  NMR (400 MHz,  $\text{CDCl}_3$ )  $\delta$  = 8.11 (td,  $J$  = 7.8, 1.8 Hz, 1H), 7.92 – 7.86 (m, 2H), 7.72 – 7.67 (m, 2H), 7.65 – 7.58 (m, 1H), 7.35 (td,  $J$  = 7.8, 1.0 Hz, 1H), 7.18 – 7.10 (m, 1H).

### *Synthesis of 9-(2-((4-bromophenyl)sulfonyl)phenyl)-9H-carbazole (2-CzSBr)*

Carbazole (0.64 g, 3.81 mmol) was dissolved in dry N,N-dimethylformamide (DMF) (20 ml), then added potassium tert-butoxide (t-BuOK) (0.46 g, 4.12 mmol). After the mixture was stirred at room temperature under a nitrogen atmosphere for 30 min, compound 2-FSBr (1.00 g, 3.17 mmol) was added into slurry, and then the mixture was stirred at 110 °C for an additional 6 h. After cooling to room temperature, the mixture was poured to 250 ml of salt water, the crude product was collected by filtration. The product was purified by silica gel column chromatography with dichloromethane/n-hexane (v/v=2:3) as eluent. Compound 2-CzSBr was obtained as a yellow solid in 81% yield (1.19 g).  $^1\text{H}$  NMR (400 MHz,  $\text{CDCl}_3$ )  $\delta$  = 8.68 – 8.61 (m, 1H), 8.10 – 8.03 (m, 2H), 7.87 – 7.78 (m, 2H), 7.28 – 7.17 (m, 5H), 6.98 – 6.92 (m, 2H), 6.90 – 6.83 (m, 2H), 6.59 – 6.52 (m, 2H).

### *Synthesis of 10-(4-((2-(9H-carbazol-9-yl)phenyl)sulfonyl)phenyl)phenyl)-10H-phenothiazine (2Cz-DPS)*

## SUPPORTING INFORMATION

Phenothiazine (0.33 g, 1.62 mmol), compound 2-CzSBr (0.5 g, 1.08 mmol), potassium tert-butoxide (t-BuOK) (0.21 g, 1.85 mmol), copper(I) iodide (11 mg, 0.06 mmol), trans-1,2-cyclohexanediamine (DACH) (0.72 mL, 0.6 mmol) were added to dry DMF (20 ml). The mixture was stirred at 150 °C for 24 h, then cooled to room temperature. The mixture was poured to 250 ml of salt water, the crude product was collected by filtration. The product was purified by silica gel column chromatography with dichloromethane/n-hexane (v/v=3:1) as eluent. Compound 2CzDPS was obtained as a white solid in 48% yield (0.30 g). <sup>1</sup>H NMR (500 MHz, DMSO-*d*<sub>6</sub>) δ = 8.53 – 8.44 (m, 1H), 8.14 (d, *J* = 7.6 Hz, 2H), 7.98 – 7.89 (m, 2H), 7.56 (dd, *J* = 7.8, 1.2 Hz, 2H), 7.42 (td, *J* = 7.8, 1.3 Hz, 2H), 7.38 – 7.33 (m, 1H), 7.29 (td, *J* = 7.7, 1.0 Hz, 2H), 7.26 – 7.18 (m, 4H), 7.15 (t, *J* = 7.4 Hz, 2H), 6.78 (d, *J* = 9.0 Hz, 2H), 6.47 (dd, *J* = 8.5, 5.7 Hz, 4H). <sup>13</sup>C NMR (126 MHz, CDCl<sub>3</sub>) δ 148.97, 143.00, 142.47, 140.61, 136.32, 134.83, 133.72, 132.54, 130.28, 129.91, 129.69, 129.50, 128.77, 127.16, 126.35, 126.16, 125.82, 123.27, 120.00, 119.63, 114.35, 110.67. EI-MS *m/z*: [m]<sup>+</sup> calcd for C<sub>36</sub>H<sub>24</sub>N<sub>2</sub>O<sub>2</sub>S<sub>2</sub>, 580, found 580. HRMS *m/z*: [m]<sup>+</sup> calcd for C<sub>36</sub>H<sub>24</sub>N<sub>2</sub>O<sub>2</sub>S<sub>2</sub>, 580.1274, found 580.1278. Anal. calcd. for C<sub>36</sub>H<sub>24</sub>N<sub>2</sub>O<sub>2</sub>S<sub>2</sub>: C 74.46, H 4.17, N 4.82, S 11.04; found: C 74.31, H 4.00, N 4.54, S 10.77.

# SUPPORTING INFORMATION

## III. Supplementary Figures

$^1\text{H}$  NMR (400 MHz,  $\text{CDCl}_3$ )  $\delta$  = 8.11 (td,  $J$  = 7.8, 1.8 Hz, 1H), 7.92 – 7.86 (m, 2H), 7.72 – 7.67 (m, 2H), 7.65 – 7.58 (m, 1H), 7.35 (td,  $J$  = 7.8, 1.0 Hz, 1H), 7.18 – 7.10 (m, 1H).

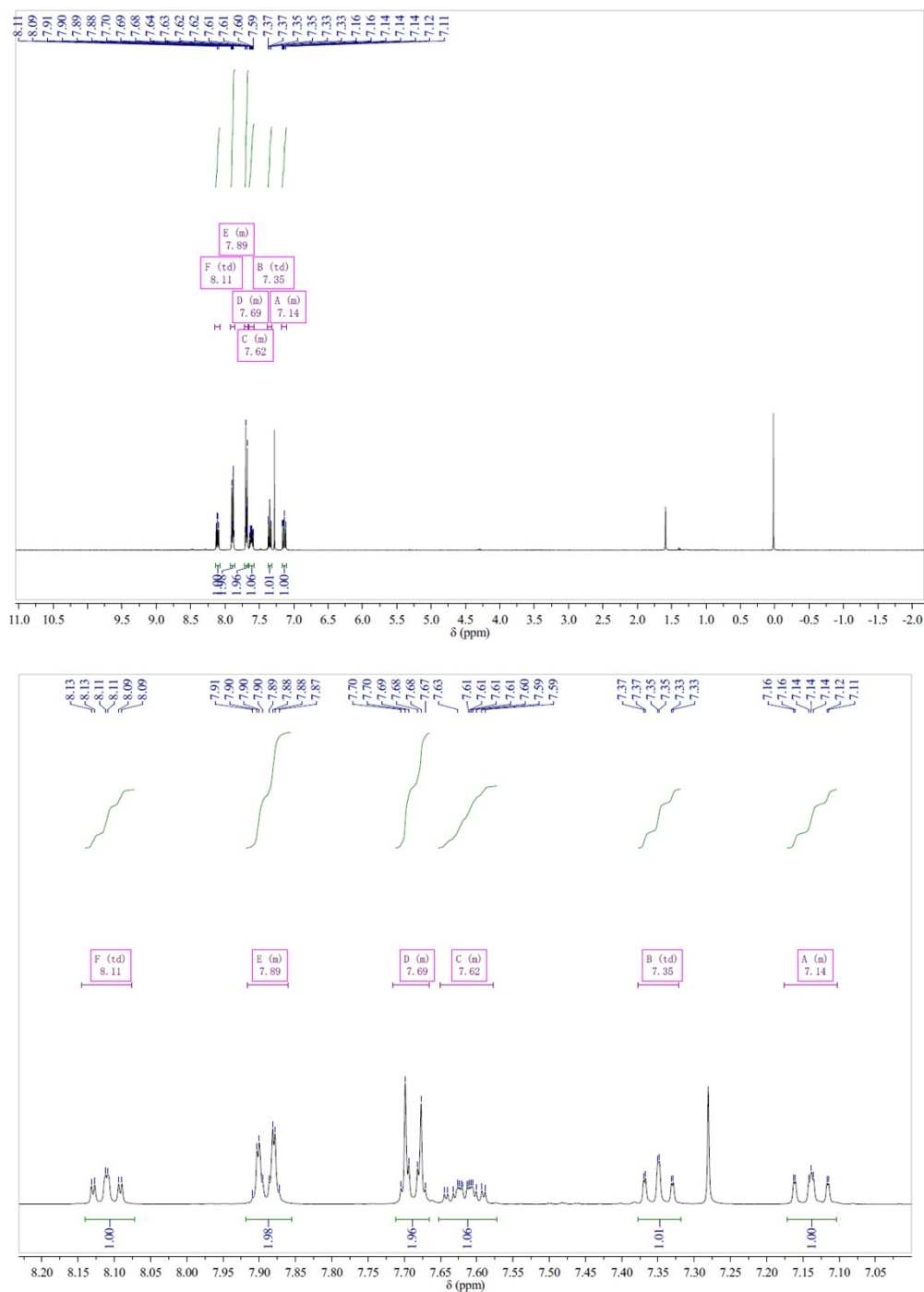


Figure S1.  $^1\text{H}$  NMR spectra of 2-FSBr.

## SUPPORTING INFORMATION

$^1\text{H}$  NMR (400 MHz,  $\text{CDCl}_3$ )  $\delta = 8.68 - 8.61$  (m, 1H),  $8.10 - 8.03$  (m, 2H),  $7.87 - 7.78$  (m, 2H),  $7.28 - 7.17$  (m, 5H),  $6.98 - 6.92$  (m, 2H),  $6.90 - 6.83$  (m, 2H),  $6.59 - 6.52$  (m, 2H).

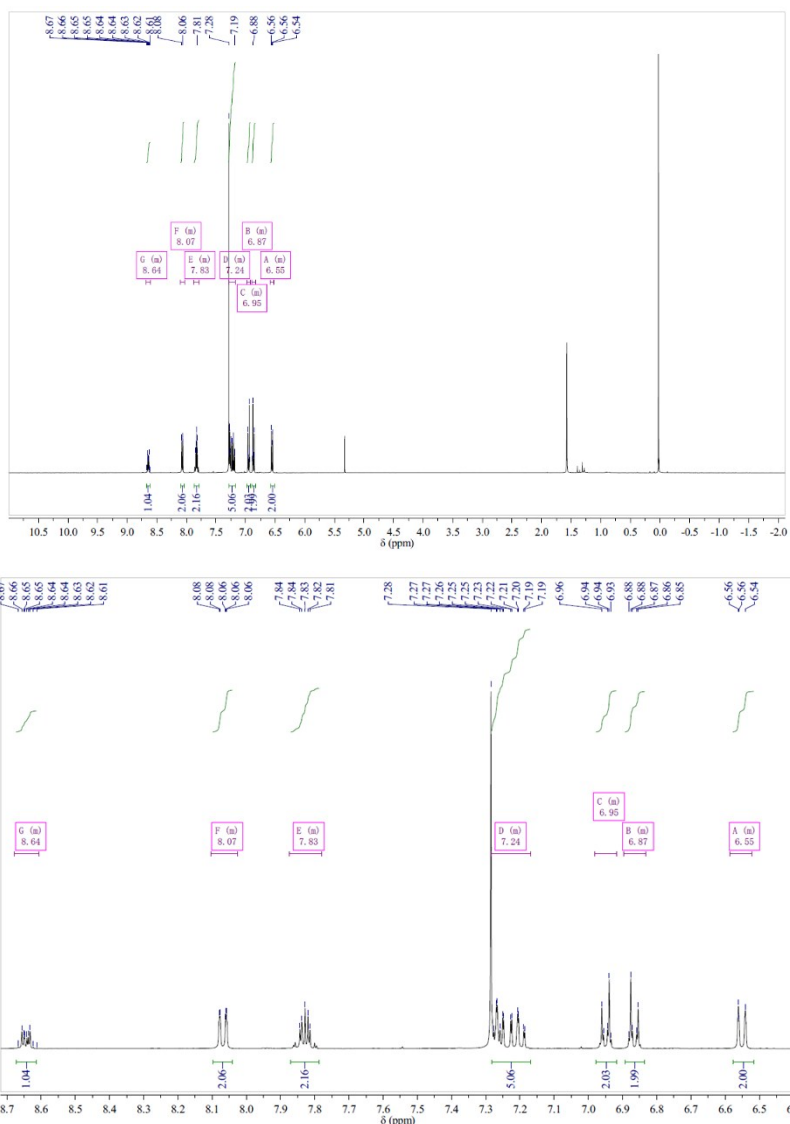


Figure S2.  $^1\text{H}$  NMR spectra of 2-CzSBr.

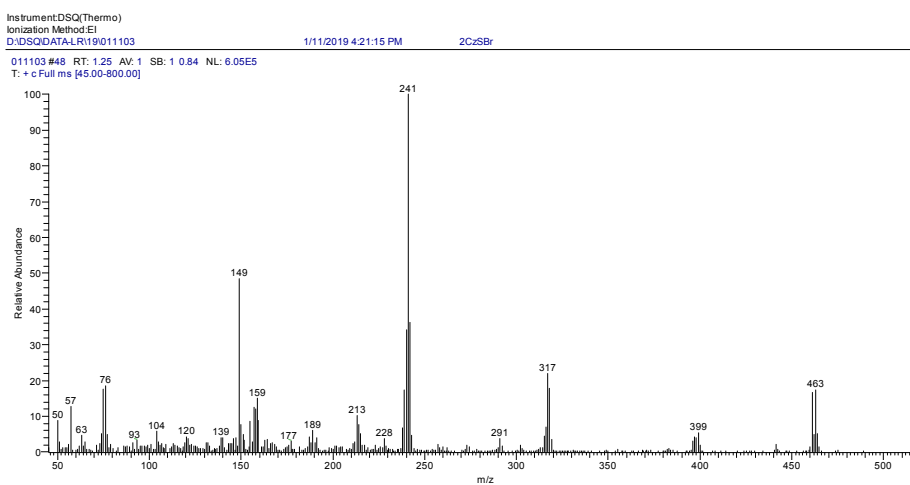
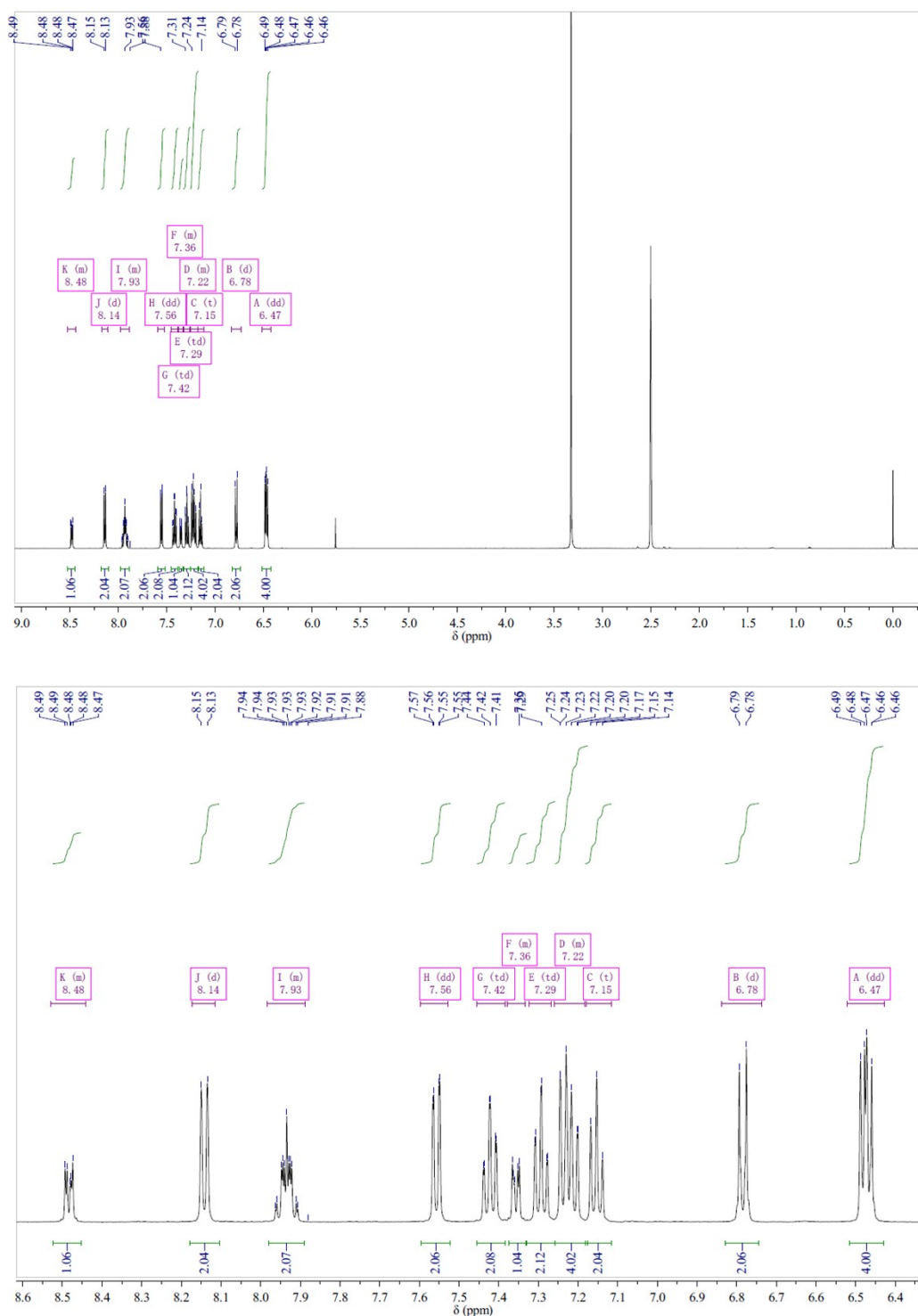


Figure S3. EI-mass spectrum of 2-CzSBr.

## SUPPORTING INFORMATION

$^1\text{H}$  NMR (500 MHz,  $\text{DMSO-}d_6$ )  $\delta$  = 8.53 – 8.44 (m, 1H), 8.14 (d,  $J$  = 7.6 Hz, 2H), 7.98 – 7.89 (m, 2H), 7.56 (dd,  $J$  = 7.8, 1.2 Hz, 2H), 7.42 (td,  $J$  = 7.8, 1.3 Hz, 2H), 7.38 – 7.33 (m, 1H), 7.29 (td,  $J$  = 7.7, 1.0 Hz, 2H), 7.26 – 7.18 (m, 4H), 7.15 (t,  $J$  = 7.4 Hz, 2H), 6.78 (d,  $J$  = 9.0 Hz, 2H), 6.47 (dd,  $J$  = 8.5, 5.7 Hz, 4H).



**Figure S4.**  $^1\text{H}$  NMR spectra of 2Cz-DPS.

$^{13}\text{C}$  NMR (126 MHz,  $\text{CDCl}_3$ )  $\delta$  = 148.97, 143.00, 142.47, 140.61, 136.32, 134.83, 133.72, 132.54, 130.28, 129.91, 129.69, 129.50, 128.77, 127.16, 126.35, 126.16, 125.82, 123.27, 120.00, 119.63, 114.35, 110.67.

# SUPPORTING INFORMATION

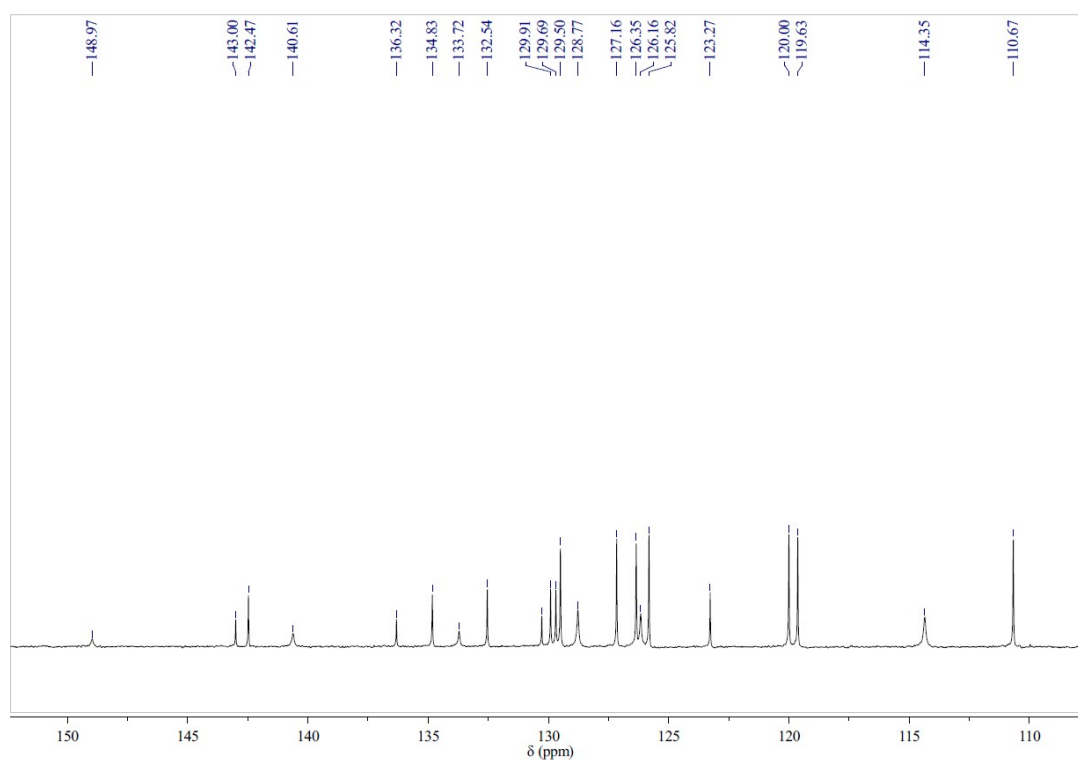
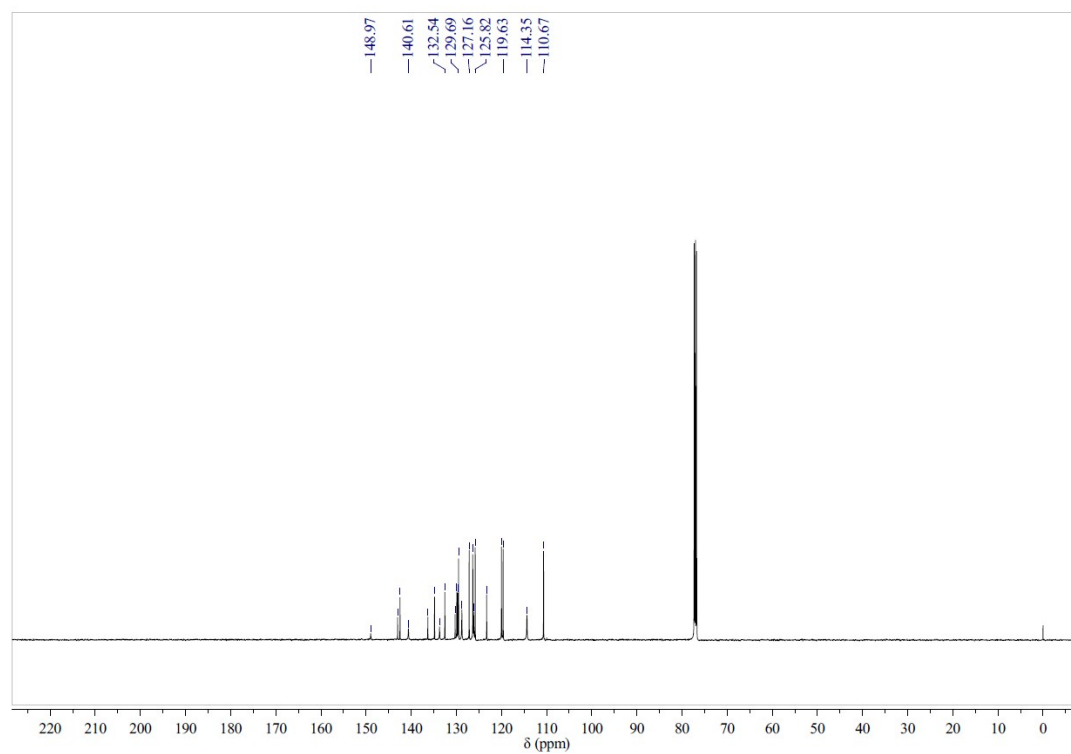


Figure S5. <sup>13</sup>C NMR spectra of 2Cz-DPS.

# SUPPORTING INFORMATION

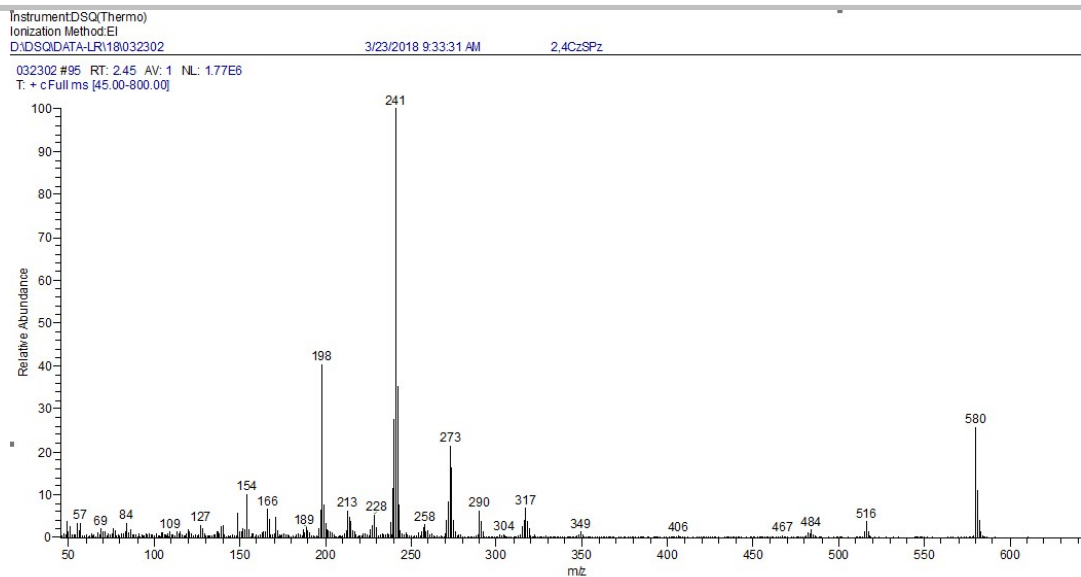


Figure S6. EI-mass spectrum of 2Cz-DPS.

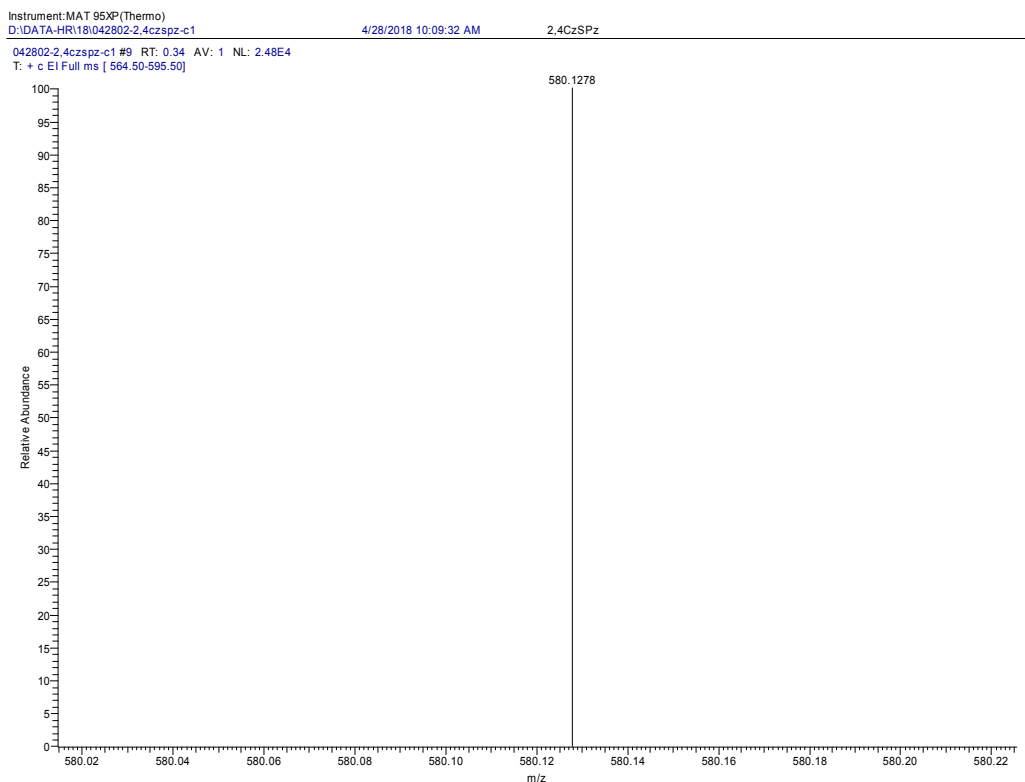


Figure S7. High resolution mass spectrum of 2Cz-DPS.

# SUPPORTING INFORMATION

Document: 20190620 CHNS test (varioELcube) from: 2019/6/21 8:29:19

CHNS元素含量分析  
varioELcube CHNS/O 元素分析仪  
serial number: 19152014

Text report

No.	Name	Weight [mg]	Method	C [%]	H [%]	N [%]	S [%]	C/N ratio	C/H ratio	Date	Time
47	2CZDPS	1.531	2mg80s	74.31	4.00	4.54	10.77	16.3835	18.5838	20.06.2019	16:51

Name: eassuperuser, Access: varioELcube superuser

2019/6/21 8:29:22

varioEL cube V3.1.8 (e638c54)2015-01-21, CHNS Mode, Ser. No.: 19152014  
Elementar Analysensysteme GmbH

**Figure S8.** CHN analytical of 2Cz-DPS.

# SUPPORTING INFORMATION

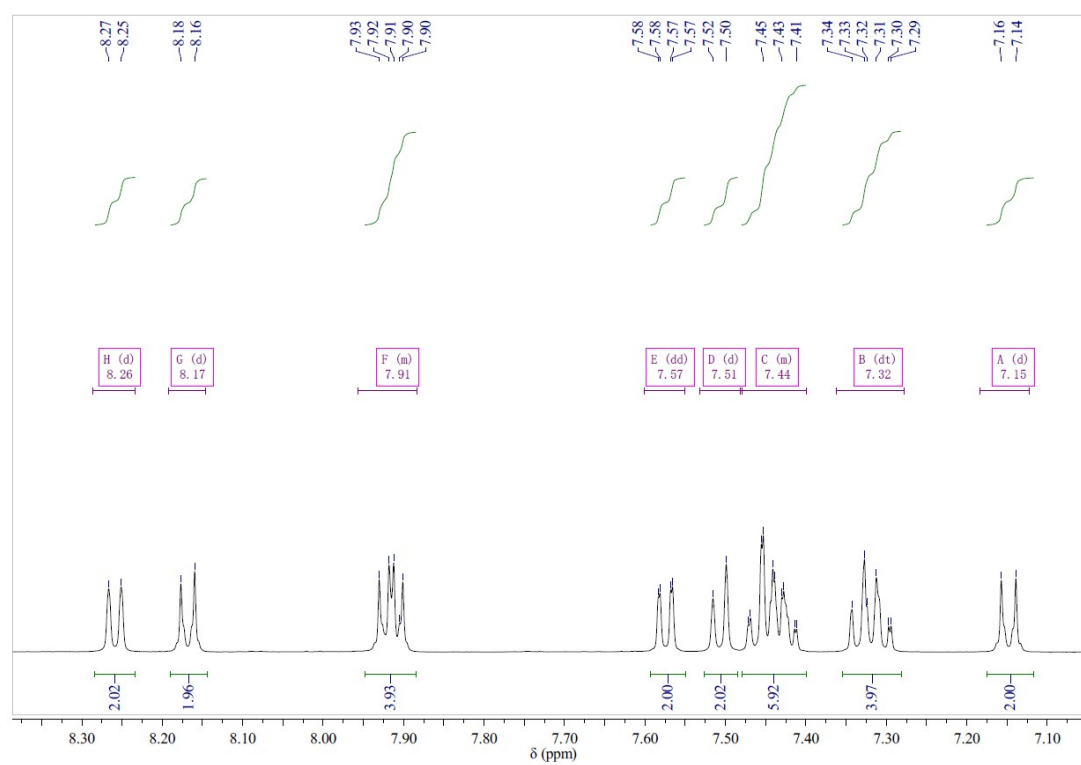
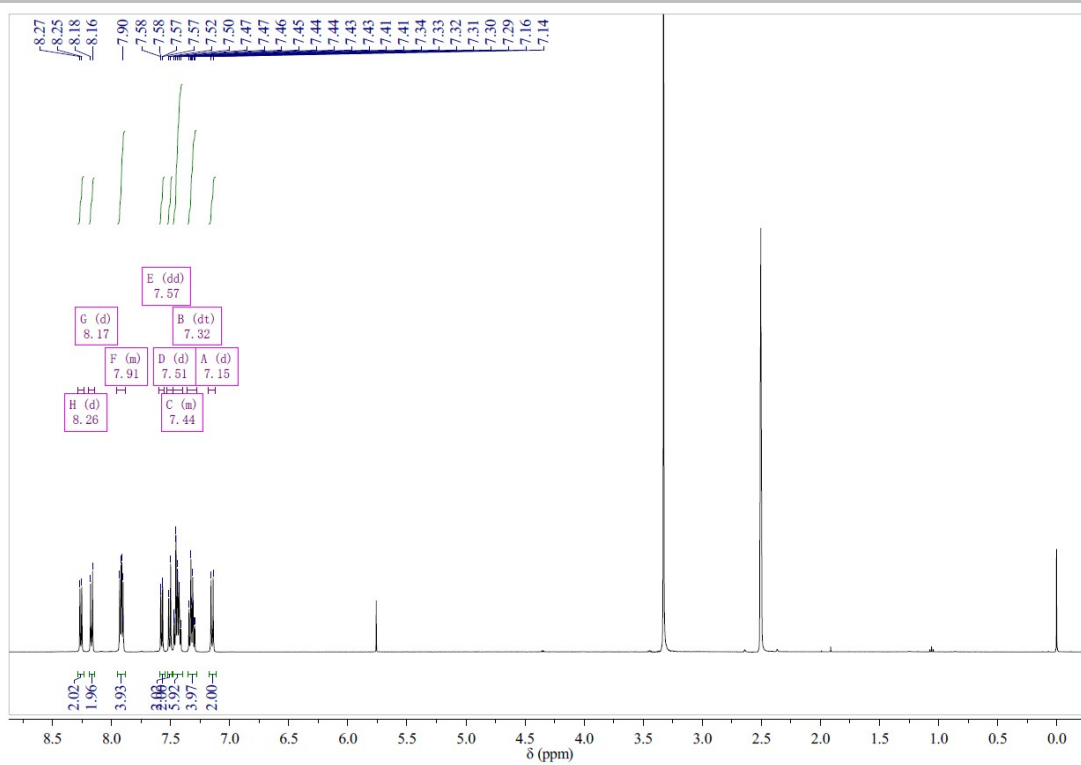


**Figure S9.**  $^1\text{H}$  NMR spectra of 4Cz-DPS.

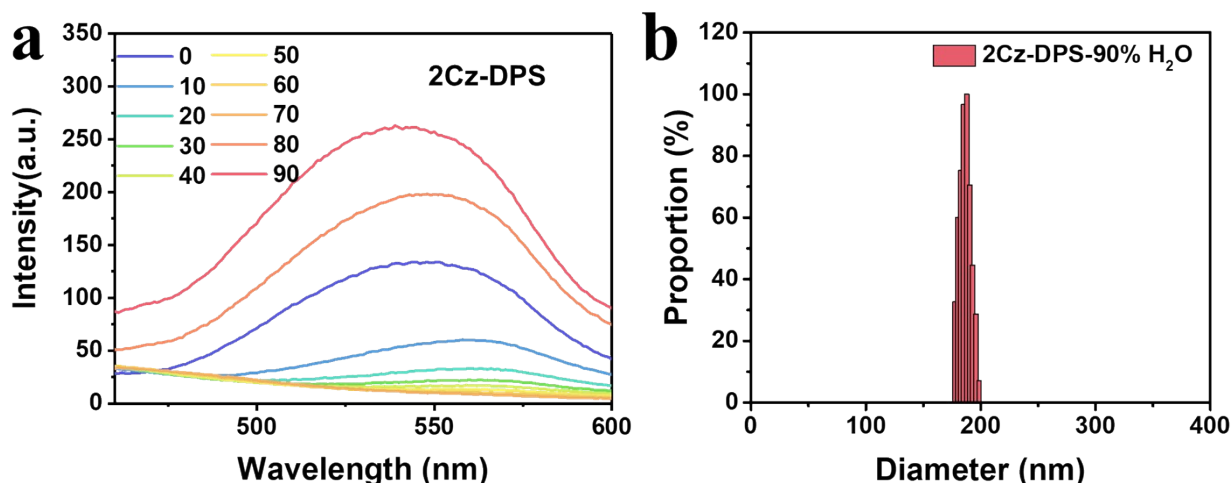


**Figure S10.** (a) PL intensity of **2Cz-DPS** as a function of water ratio (%). (b) Effective diameters of **2Cz-DPS** nanoaggregates in H<sub>2</sub>O/THF mixtures with 90% water ratio.

As seen from the THF/water solutions with different water ratios ( $f_w$ ) (Figure S10a), the solutions of **2Cz-DPS** with low water ratios give very weak emission, while highly intense green emission is observed when a large amount of water ( $f_w = 90\%$ ) is added. In THF solutions, the flexible phenothiazine moiety can consume the excited energy through conformation vibrations, resulting in the weak emission. However, in aggregated states with the formation of nanoaggregates by adding water, the molecular vibrations can be suppressed, leading to intensified light emission. Additional evidence for the nanoaggregates is from dynamic light scattering (DLS) studies on the solution of **2Cz-DPS** in 90% water/THF (v/v) (Figure S10b), showing the nanoaggregates with effective diameters of 186 nm.

Indeed, this effect of solvent polarity on optical properties makes verifying the AIE phenomenon rather difficult since most of the solvents used in the archetypal “THF-water” experiment, in which small volume amounts of water are added gradually to a THF solution until a precipitation results in a large enhancement in the emission intensity, are polar in nature, i.e., tetrahydrofuran. Additionally, as pointed out in our recent study,<sup>[5]</sup> it is the polarity solvent that is responsible for the reduction in emission and red-shifts in the dilute solution state rather than excessive internal motions affecting the fluorescence. As a result, typical AIE characteristics unearthed by traditional methods are unsuitable. Therefore, PLQY measurements in dilute non-polar hexane, which would minimize the CT stabilization, was conducted for both **2Cz-DPS** and **4Cz-DPS**, in which both **2Cz-DPS** and **4Cz-DPS** exhibit near quenching with PLQYs of 0.9% and 1%, respectively. Compared to the extremely high PLQYs in the solid-state of 91.9% and 97.3% for **2Cz-DPS** and **4Cz-DPS**, respectively, it is quite clear that these fluorophores do exhibit AIE effect, which suggests these efficient emitters have a high potential to be used as the non-doped emissive layers in TADF-based OLEDs.

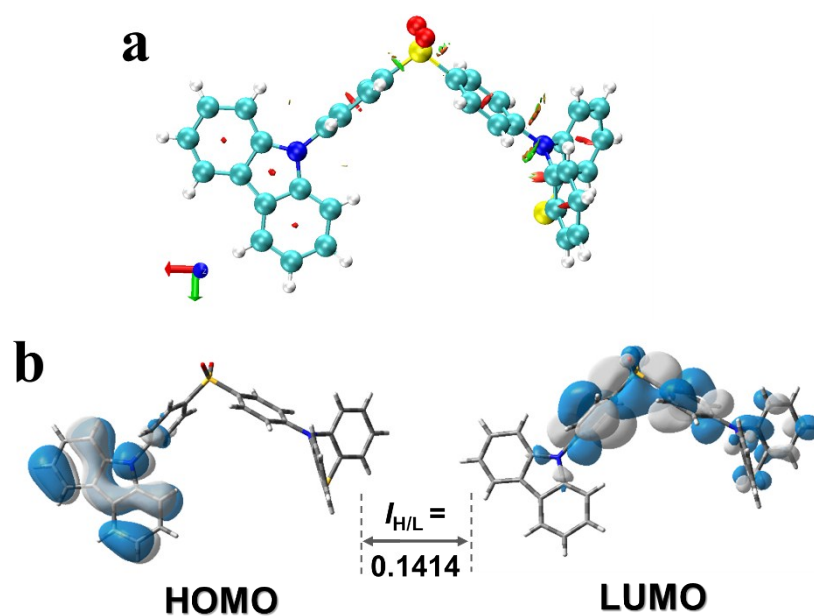


Figure S11. (a) Reduced density gradient (RDG) isosurface map with isovalue of 0.5, and (b) HOMO and LUMO distribution of 4Cz-DPS, showing the overlap integral extents  $I_{H/L}$ .

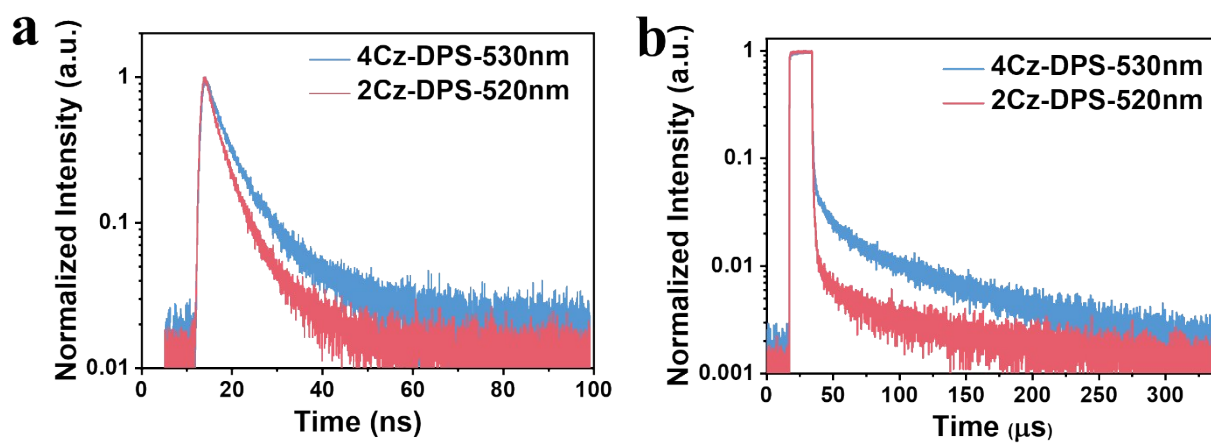
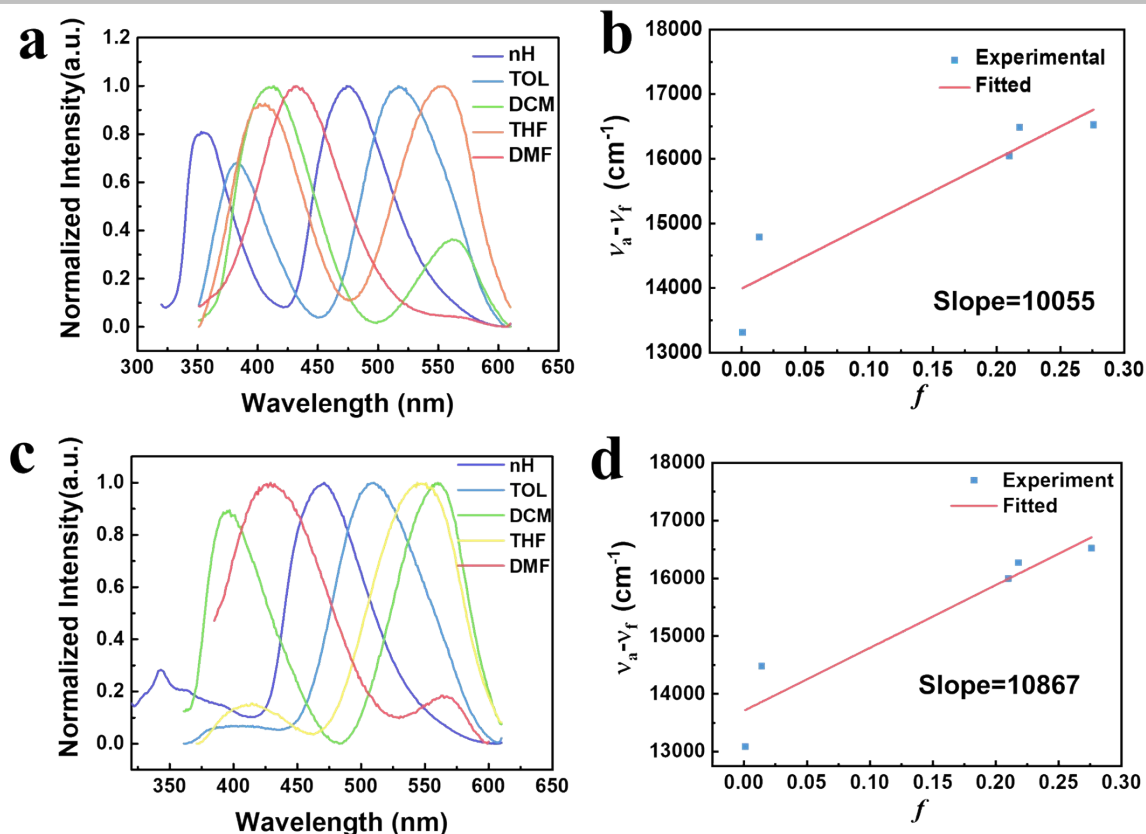
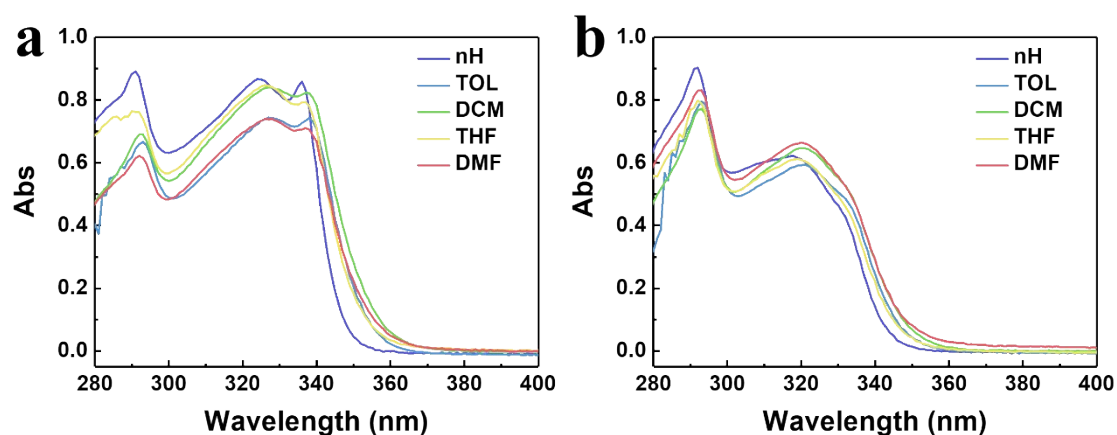


Figure S12. (a) Transient and (b) delayed curves of 4Cz-DPS and 2Cz-DPS films.

## SUPPORTING INFORMATION



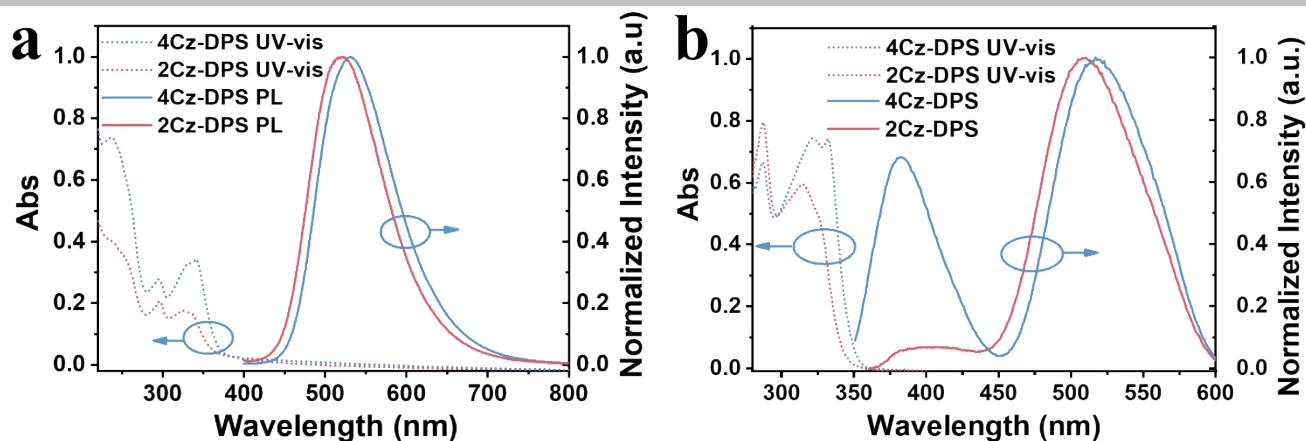
**Figure S13.** PL spectra of (a) **4Cz-DPS** and (c) **2Cz-DPS** in different solvents. Linear correlation of orientation polarization ( $f$ ) of solvent media with the Stokes shift ( $\nu_a - \nu_f$ ) for (b) **4Cz-DPS** and (d) **2Cz-DPS**.



**Figure S14.** UV-vis absorption spectra of (a) **4Cz-DPS** and (b) **2Cz-DPS** in different solvents.

The effect of solvent polarity on the optical properties of **4Cz-DPS** and **2Cz-DPS** was investigated. It was found that their PL spectra demonstrated a large dependence on the solvent polarity, and presented large Stokes shifts with increasing the solvent polarity (Figure S13). The emission peaks of **4Cz-DPS** and **2Cz-DPS** are red-shifted gradually while the solvent polarity arises, verifying the CT character of the green emission.<sup>[6]</sup> On the contrary, the absorption spectra of **4Cz-DPS** and **2Cz-DPS** are relatively insensitive to the solvent polarity (Figure S14).

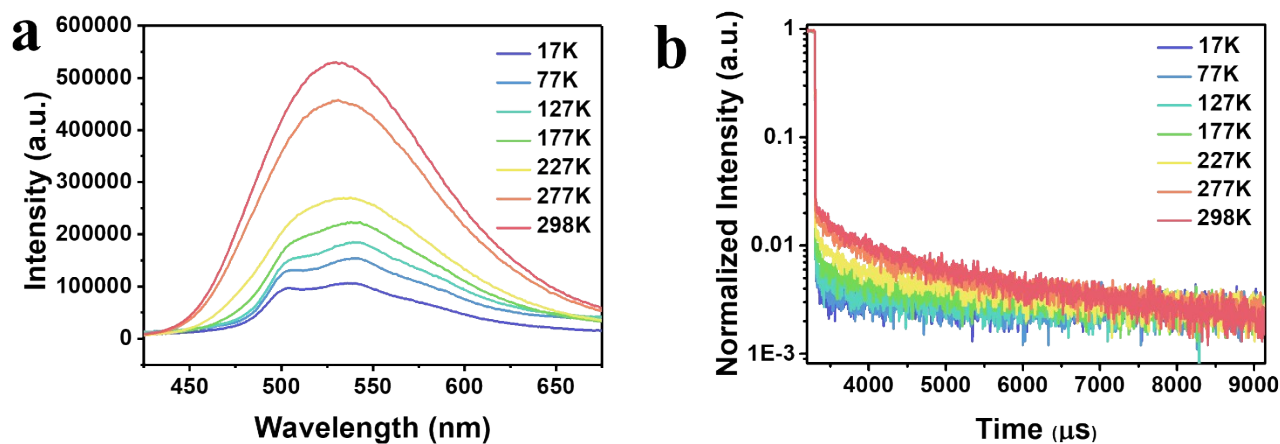
## SUPPORTING INFORMATION



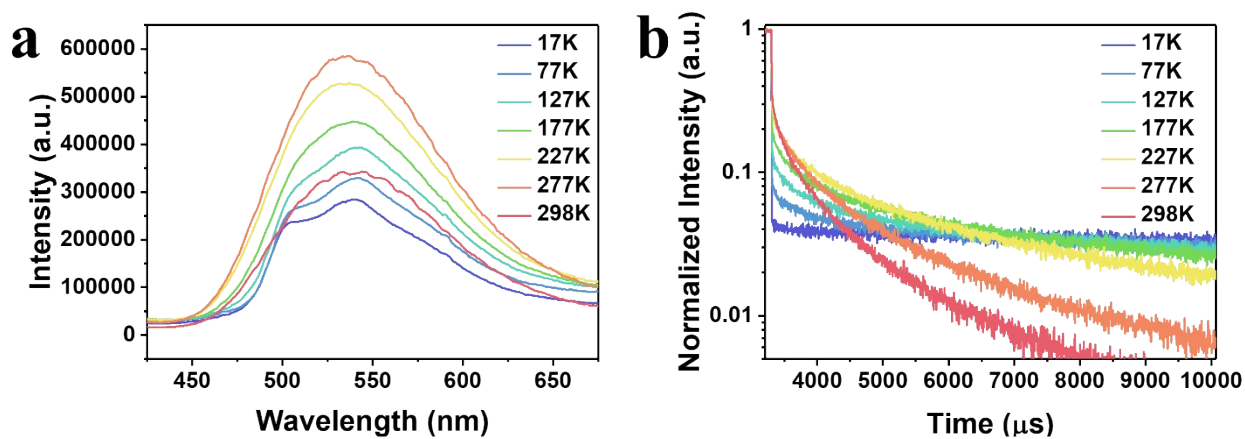
**Figure S15.** UV-vis absorption and PL spectra of **4Cz-DPS** and **2Cz-DPS** in (a) neat films and (b) THF solutions.

Figure S15a shows the UV-vis absorption spectra and PL spectra of **4Cz-DPS** and **2Cz-DPS** films. The two compounds have similar absorption behaviors, the absorption bands 230 – 270 nm and 270 – 300 nm are attributed to  $\pi$ - $\pi^*$  transitions of the diphenyl-sulfone and carbazole groups, respectively, while the absorption band 310 – 400 nm is ascribed to the intramolecular CT transition. The PL emission of **4Cz-DPS** and **2Cz-DPS** films give structure-less spectra centered at 530 nm and 520 nm, respectively. In comparison to **4Cz-DPS**, **2Cz-DPS** demonstrates a blue-shifted PL spectrum, owing to its more rigid molecular structure. Different from that in neat film, the emission behavior of **2Cz-DPS** in THF solution presents dual peaks (Figure S15b) due to conformation changes of the phenothiazine unit.<sup>[7]</sup> In contrast to the PL spectra in the solutions, the absence of short wavelength range for the PL spectra in the films is due to highly strengthened and dominated intermolecular CT process in the solid-state films.<sup>[8]</sup>

## SUPPORTING INFORMATION



**Figure S16.** (a) Temperature dependent steady-state spectra and (b) transient PL decay curves of **2Cz-DPS** films carried out at different temperatures.



**Figure S17.** (a) Temperature dependent steady-state spectra and (b) transient PL decay curves of **4Cz-DPS** films carried out at different temperatures.

## SUPPORTING INFORMATION

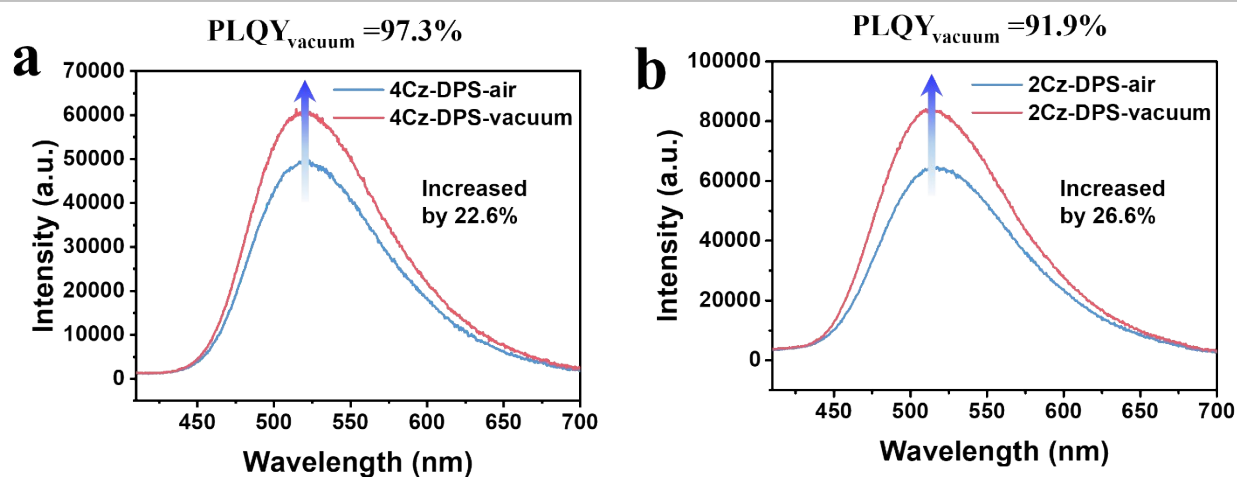


Figure S18. PL spectra of (a) **4Cz-DPS** and (b) **2Cz-DPS** films in air and vacuum.

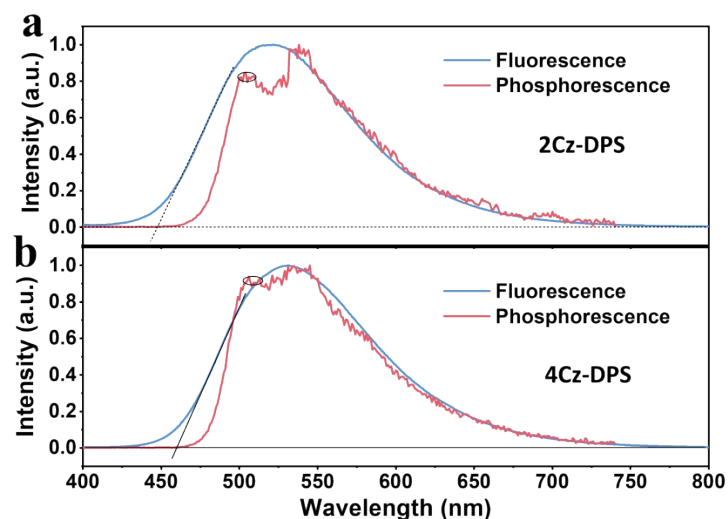


Figure S19. Fluorescence spectra at room temperature and phosphorescence spectra at 77 K for **4Cz-DPS** and **2Cz-DPS** films.

The singlet ( $S_1$ ) and triplet ( $T_1$ ) energy level of **4Cz-DPS** and **2Cz-DPS** films are evaluated from the onset of fluorescence spectra at room temperature and the peak of phosphorescence spectra at 77 K, respectively. As a result, the energy level of  $S_1$  is identified to be 2.70 eV for **4Cz-DPS** and 2.78 eV for **2Cz-DPS**, and the energy level of  $T_1$  is examined to be 2.45 eV for **4Cz-DPS** and 2.46 eV for **2Cz-DPS**.

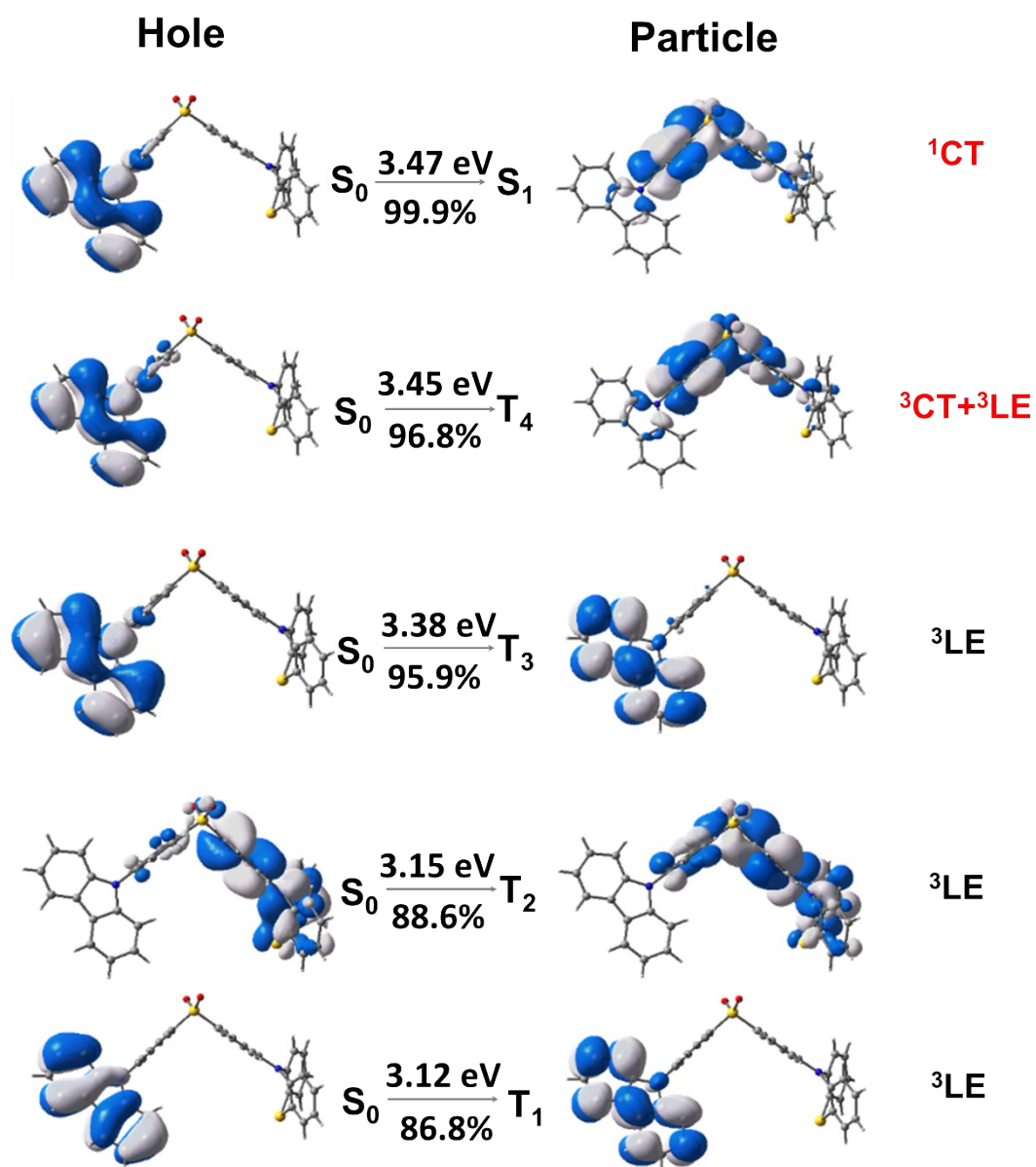


Figure S20. Natural transition orbitals of 4Cz-DPS for the  $S_0$ ,  $S_1$ ,  $T_1$ ,  $T_2$ ,  $T_3$  and  $T_4$  states.

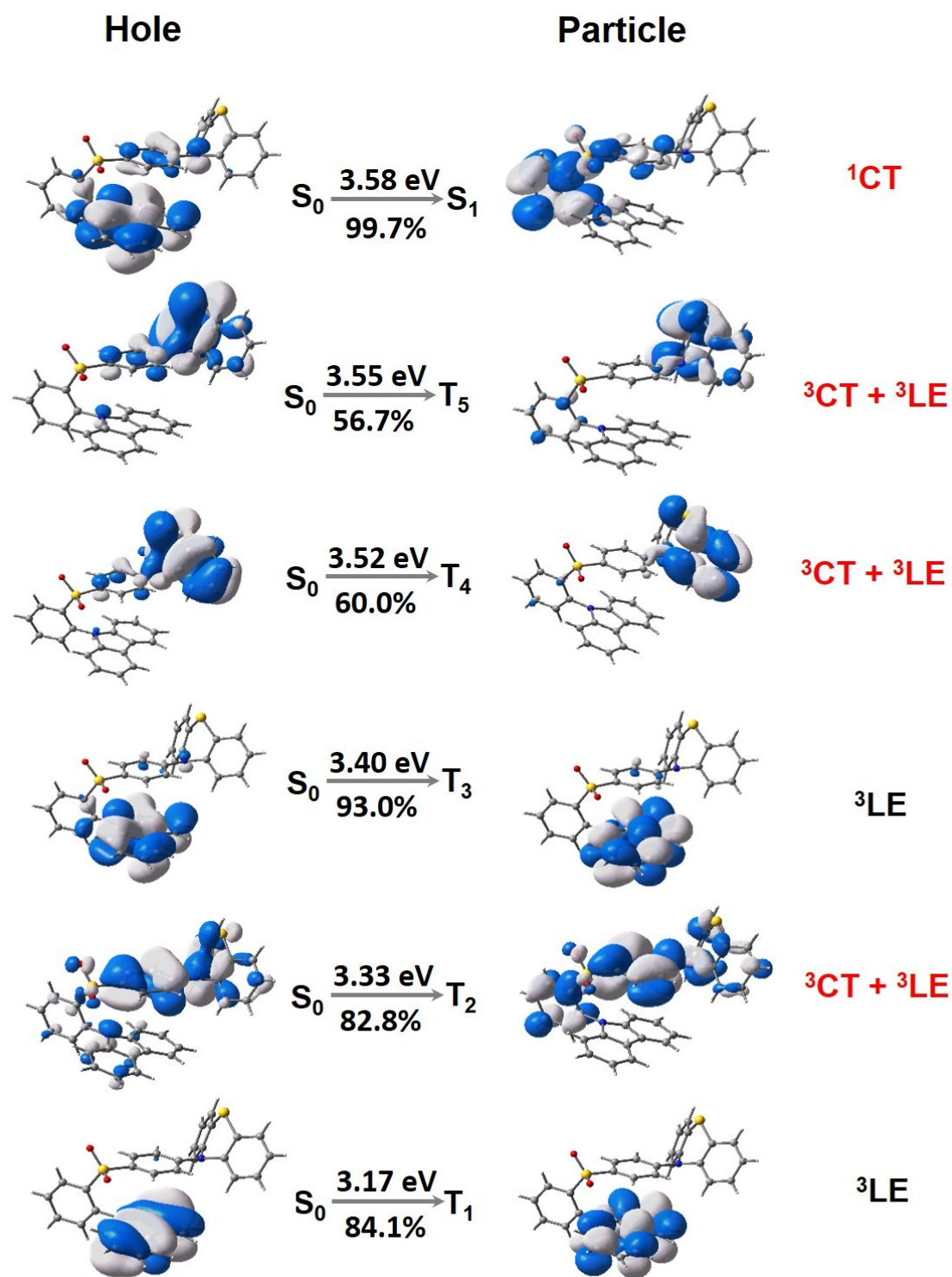
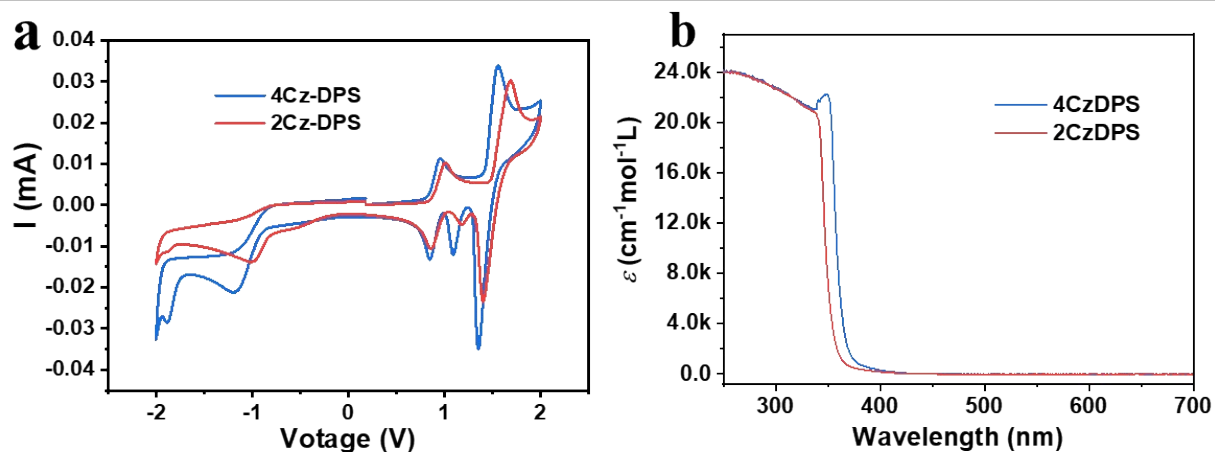
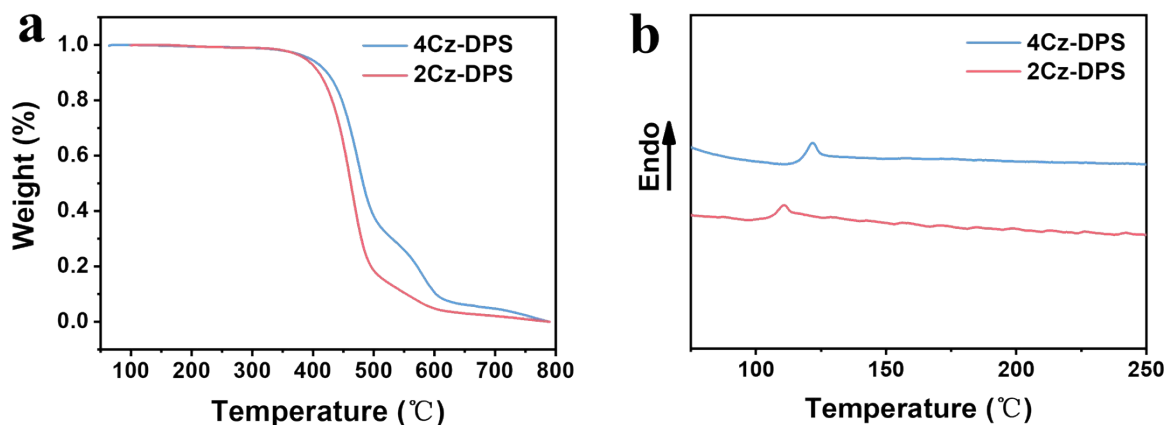


Figure S21. Natural transition orbitals of 2Cz-DPS for the  $S_0$ ,  $S_1$ ,  $T_1$ ,  $T_2$ ,  $T_3$ ,  $T_4$  and  $T_5$  states.

## SUPPORTING INFORMATION



**Figure S22.** (a) Cyclic voltammety measurements of **4Cz-DPS** and **2Cz-DPS**. HOMO is determined by  $\text{HOMO} = -4.8 - (E_{\text{ox}} - E_{1/2(\text{Ferrocene})})$ ,<sup>[9]</sup> where  $E_{\text{ox}}$  is the oxidation potential point,  $E_{1/2(\text{Ferrocene})}$  is the oxidation potential of ferrocene ( $\text{F}_0/\text{F}_c^+$ ). (b) UV-vis absorption spectra in DCM solutions ( $5 \times 10^{-4}$  mol/L) of **4Cz-DPS** and **2Cz-DPS**.



**Figure S23.** (a) Thermogravimetric analysis curves and (b) differential scanning calorimetry curve of **4Cz-DPS** and **2Cz-DPS** measured under  $\text{N}_2$ , showing the glass transition temperature ( $T_g$ ).

## SUPPORTING INFORMATION

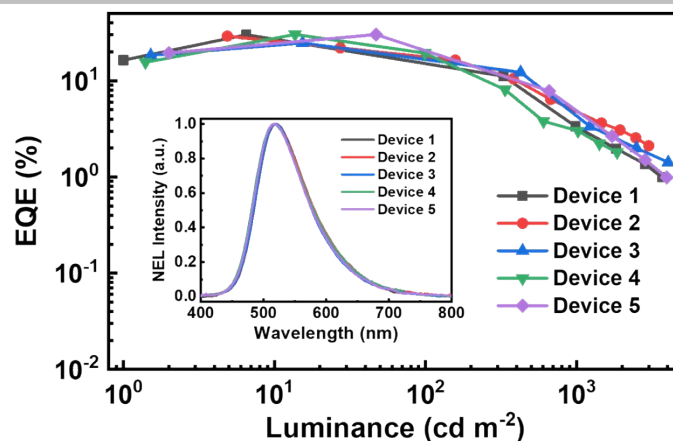


**Figure S24.** EQE–luminance curves of other five **2Cz-DPS** devices. Inset: normalized EL spectra.

In order to prove that the device performance of **2Cz-DPS**-based non-doped OLEDs has good reproducibility, other five devices were fabricated with the same device configuration: ITO/PEDOT:PSS (30 nm)/MCP (20 nm)/ **2Cz-DPS** (30 nm)/TPBI (40 nm)/LiF(1 nm)/Al (100 nm), which was also the same as that of the **2Cz-DPS** device presented in the manuscript. As seen from **Figure S24**, the maximum EQEs obtained from these five OLEDs were: 30.2% (device 1), 29.2% (device 2), 24.8% (device 3), 30.4% (device 4) and 30.3% (device 5), and all the devices presented the same EL spectra with a peak at 520 nm. The results convincingly demonstrate high efficiency of **2Cz-DPS** as TADF emitter and also good reproducibility of high device performance from **2Cz-DPS**-based OLEDs.

## SUPPORTING INFORMATION

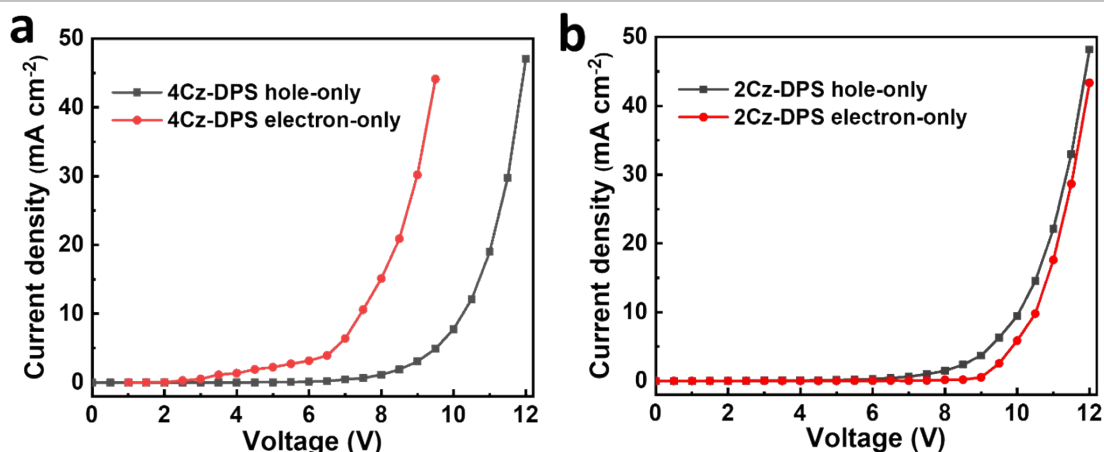


**Figure S25.** Current density–voltage curves of (a) **4Cz-DPS** and (b) **2Cz-DPS** based single carrier devices. The hole-only device is: ITO/MoO<sub>3</sub>(5 nm)/**4Cz-DPS** or **2Cz-DPS** (100 nm)/MoO<sub>3</sub>(5 nm)/Al(100 nm), and the electron-only device is: ITO/LiF(5 nm)/**4Cz-DPS** or **2Cz-DPS** (100 nm)/LiF(5 nm)/Al(100 nm).

According to the field-dependent space charge-limited current model,<sup>[10]</sup> the hole mobilities of **4Cz-DPS** and **2Cz-DPS** reach the same level ( $10^{-7} \text{ cm}^2 \text{ V}^{-1} \text{ s}^{-1}$ ), as estimated from the  $J$ - $V$  curves of the single carrier devices. However, the electron mobility of **4Cz-DPS** ( $10^{-6} \text{ cm}^2 \text{ V}^{-1} \text{ s}^{-1}$ ) is an order higher than that of **2Cz-DPS** ( $10^{-7} \text{ cm}^2 \text{ V}^{-1} \text{ s}^{-1}$ ). Consequently, a higher charge carrier balance ratio is expected in **2Cz-DPS** device, which should mainly be responsible for its higher efficiencies, considering the other three factors determining EQEs behavior similarly for **4Cz-DPS** and **2Cz-DPS**, including the PLQY ( $\sim 100\%$ ), singlet/triplet excitons utilization efficiency ( $\eta_{ST}$ , 100%) and out-coupling efficiency ( $\eta_{\text{out}}$ ,  $\sim 30\%$ ).<sup>[11]</sup>

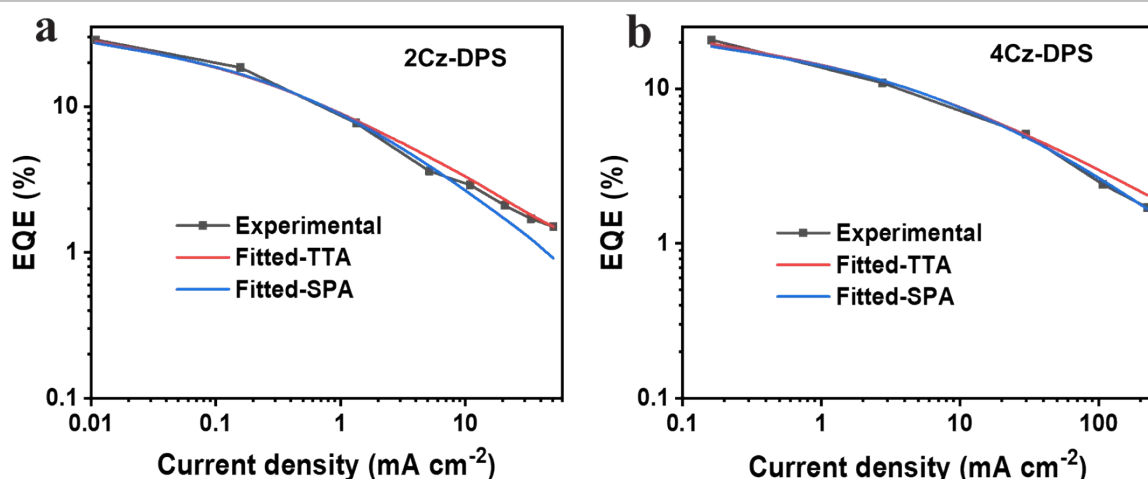


**Figure S26.** EQE–current density curve simulation for (a) 2Cz-DPS device and (b) 4Cz-DPS device. The fitting results are based on triplet-triplet annihilation (TTA) and singlet-polaron annihilation (SPA) models.

We investigated the efficiency roll-off behaviors by taking both triplet-triplet annihilation (TTA) and singlet-polaron annihilation (SPA) into account. The TTA model represents an exciton-exciton quenching process, while the SPA model is related to exciton-polaron (charged molecules) process, and the current density dependent EQE in the TTA and SPA models is expressed by equation (1) and (2) respectively:<sup>[12]</sup>

$$\frac{\eta_{TT}}{\eta_0} = \frac{J_0}{4J} \left( \sqrt{1 + \frac{8J}{J_0}} - 1 \right) \quad (1)$$

$$\frac{\eta_{SP}}{\eta_0} = \frac{1}{1 + \left( \frac{J}{J_0} \right)^{\frac{1}{1+m}}} \quad (2)$$

where  $\eta_{TT}$  and  $\eta_{SP}$  is the EQE in the presence of TTA and SPA respectively,  $\eta_0$  is the maximum EQE,  $J_0$  is the current density where EQE reaches half of the maximum value, and  $m$  is the fitting parameter.

#### IV. References

- [1] S. Xu, T. Liu, Y. Mu, Y.-F. Wang, Z. G. Chi, C.-C. Lo, S. Liu, Y. Zhang, A. Lien, J. R. Xu, *Angew. Chem. Int. Ed.* **2015**, *54*, 874–878.
- [2] B. Xu, Y. Mu, Z. Mao, Z. Xie, H. Wu, Y. Zhang, C. Jin, Z. G. Chi, S. Liu, J. R. Xu, Y.-C. Wu, P.-Y. Lu, A. Lienc, M. R. Bryce, *Chem. Sci.* **2016**, *7*, 2201–2206.
- [3] S. R. Forrest, D. D. C. Bradley, M. E. Thompson, *Adv. Mater.* **2003**, *15*, 1043–1048.
- [4] a) Y. Tao, K. Yuan, T. Chen, P. Xu, H. Li, R. Chen, C. Zheng, L. Zhang, W. Huang, *Adv. Mater.* **2014**, *26*, 7931–7958; b) Q. Zhang, H. Kuwabara, W. J. Potscavage, Jr., S. Huang, Y. Hatae, T. Shibata, C. Adachi, *J. Am. Chem. Soc.* **2014**, *136*, 18070–18081.

## SUPPORTING INFORMATION

- [5] M. Aydemir, S. D. Xu, C. J. Chen, M. R. Bryce, Z. G. Chi, A. P. Monkman, *J. Phys. Chem. C* **2017**, *121*, 17764–17772.
- [6] A. Wakamiya, K. Mori, S. Yamaguchi, *Angew. Chem. Int. Ed.* **2007**, *46*, 4273–4276.
- [7] I. Marghad, F. Bencheikh, C. Wang, S. Manolikakes, A. Rerat, C. Gosmini, D. H. Kim, J.-C. Ribierre, C. Adachi, *RSC Adv.* **2019**, *9*, 4336–4343.
- [8] a) Z. Xie, C. Chen, S. Xu, J. Li, Y. Zhang, S. Liu, J. R. Xu, Z. G. Chi, *Angew. Chem. Int. Ed.* **2015**, *54*, 7181–7184; b) Z. L. Xie, Q. Y. Huang, T. Yu, L. Y. Wang, Z. Mao, W. L. Li, Z. Yang, Y. Zhang, S. W. Liu, J. R. Xu, Z. G. Chi, M. P. Aldred, *Adv. Funct. Mater.* **2017**, 1703918.
- [9] Q. Li, Y. Yuan, T. Wei, Y. Li, Z. Chen, X. Jin, Y. Qin, W. Sun, *Sol. Energ. Mater. Sol. Cells* **2014**, *130*, 426–434.
- [10] a) P. N. Murgatroyd, *J. Phys. D: Appl. Phys.* **1970**, *3*, 151–156; b) G. Lin, H. Peng, L. Chen, H. Nie, W. Luo, Y. Li, S. Chen, R. Hu, A. J. Qin, Z. J. Zhao, B. Z. Tang, *ACS Appl. Mater. Interfaces* **2016**, *8*, 16799–16808.
- [11] H. Kaji, H. Suzuki, T. Fukushima, K. Shizu, K. Suzuki, S. Kubo, T. Komino, H. Oiwa, F. Suzuki, A. Wakamiya, Y. Murata, C. Adachi, *Nat. Commun.* **2015**, *6*, 8476.
- [12] a) S. Ying, D. Yang, X. Qiao, Y. Dai, Q. Sun, J. Chen, T. Ahamad, S. M. Alshehri, D. Ma. *J. Mater. Chem. C*, **2018**, *6*, 10793–10803; b) C. Li, L. Duan, D. Zhang, Y. Qiu, *ACS Appl. Mater. Interfaces* **2015**, *7*, 15154–15159.

### Author Contributions

Juan Zhao, Zhiyong Yang, Yi Zhang, Jiarui Xu and Zhenguo Chi designed the experiments.

Zhan Yang, Zhu Mao, and Xiaojie Chen performed the experiments.

Chao Xu and Zhu Mao carried out the theoretical simulations.

All the authors were involved in the analysis and interpretation of data.

Zhan Yang, Zhu Mao wrote the manuscript with the help of Juan Zhao, Yi Zhang, Zhenguo Chi and Matthew. P. Aldred.

Zhan Yang and Zhu Mao contributed equally to this work.